ISSN 0021-3640, JETP Letters, 2021, Vol. 113, No. 5, pp. 308–316. © Pleiades Publishing, Inc., 2021.
Russian Text © The Author(s), 2021, published in Pis'ma v Zhurnal Eksperimental'noi i Teoreticheskoi Fiziki, 2021, Vol. 113, No. 5, pp. 311–319.

OPTICS
AND LASER PHYSICS

Femtosecond Laser Irradiation of a Multilayer Metal–Metal Nanostructure

S. A. Romashevskiy[a, *], V. A. Khokhlov[b], S. I. Ashitkov[a], V. V. Zhakhovsky[a, c], N. A. Inogamov[a, b, c], P. S. Komarov[a], A. N. Parshikov[a, c], Yu. V. Petrov[b, d], E. V. Struleva[a], and P. A. Tsygankov[e]

[a] *Joint Institute for High Temperatures, Russian Academy of Sciences, Moscow, 125412 Russia*
[b] *Landau Institute for Theoretical Physics, Russian Academy of Sciences, Chernogolovka, Moscow region, 142432 Russia*
[c] *All-Russia Research Institute of Automatics, Moscow, 127055 Russia*
[d] *Moscow Institute of Physics and Technology (National Research University), Dolgoprudnyi, Moscow region, 141701 Russia*
[e] *Universidad Industrial de Santander, 680003 Bucaramanga, Colombia*
**e-mail: sa.romashevskiy@gmail.com*

Received November 26, 2020; revised January 24, 2021; accepted January 25, 2021

The selective modification of upper layers of a Ni/Al multilayer nanostructure irradiated by a single femtosecond laser pulse has been studied. The analysis of surface topography indicates that either partial or complete removal of two upper layers is possible depending on the absorbed energy. The surface has been scanned by an atomic force microscope. The numerical simulation of the phenomenon with a two-temperature hydrodynamic code has revealed an asynchronous dynamics of the electron subsystems of Ni and Al and an inhomogeneous heating of ion subsystems. As a result, a complex combination of compression and rarefaction waves is initiated in the multilayer target. It has been shown numerically that, as the absorbed energy increases, the first nickel layer is initially ruptured because of the localization of tensile stresses. The experimental and numerical thicknesses of the separated layer and the threshold energy are in agreement with each other. Consequently, the parameters of two-temperature models of nickel and aluminum are selected correctly.

DOI: 10.1134/S002136402105009X

INTRODUCTION

Multilayer structures (nanolaminates) consist of alternating nanolayers of two or more materials. Nanolaminates are widely used in many fields of modern engineering such as microelectronics, mirrors for focusing of soft monochromatic X rays (modern photolithography), photovoltaic devices for solar power engineering, plasmonics, and magnetoplasmonics [1–5]. Significant progress has been achieved in recent years in the selective modification of multilayer nanomaterials by femtosecond laser pulses for such applications [6–9].

The heating of a metal by femtosecond laser pulses with a moderate intensity of $\sim 10^{12}$–10^{13} W/cm^2 transfers the metal to a two-temperature state with the hot electron and cold ion subsystems. Processes of electron–ion thermalization, heat transfer, and melting of the surface layer are accompanied by acoustic phenomena: the nucleation, propagation, and interference of compression and rarefaction waves with the subsequent formation of intense tensile stresses. Above the strength threshold, tension results in the separation of a thin surface layer and the formation of an ablation crater on the surface [10–14]. The sizes of the thermal effect region of femtosecond laser pulses are minimal, which is important for the development of technologies of processing of promising film nanomaterials.

Problems of selective laser processing of nanolaminates are still insufficiently studied (see the last paragraph of the Introduction) because of the diversity of thermodynamic and mechanical properties of neighboring layers, variation of the interlayer adhesion, and interface thermal resistance. All these properties significantly affect the results of micro/nanoprocessing, e.g., the possibility of selective removal of required layers. Features of the transport and relaxation of the absorbed energy, as well as the interference of acoustic waves reflected from interfaces, lead to a complex morphology of modified layers.

At close acoustic impedances, as in the Si/Al semiconductor–metal structure [15], rupture occurred at interfaces because the adhesion of the layers is smaller than their bulk strength. The situation is much more complicated in the case of different impedances and strong adhesion (as in metal–metal systems). In this case, the thermodynamic and transport properties of the layers, as well as the sequence of their alternation,

are important according to [16–20], where Ti/Al, Ni/Ti, and Ag/Cu systems were studied in detail.

Experiments reported in [21] demonstrated that spallation inside a Ni film (with a thickness of several tens of nanometers) occurs before the separation of the film from the substrate. Partial spallation at a depth of 7–10 nm was detected in a 20-nm film (the minimum depth of the crater in a bulk nickel target is 20 nm).

Interest in laser action of Ni/Al nanolaminate is due not only to the above applications (electronics, lithography, and photovoltaics) but also to exothermic reactions producing NiAl, $NiAl_3$, and Ni_3Al intermetallic compounds [22, 23]. For this reason, such nanolaminate can be considered as an energy-producing material. A reaction proceeds during diffuse mixing at the interface between nickel and aluminum and produces an atomic alloy. The alloy decays into intermetallic crystallites. The heat of the reaction is significant but is noticeably smaller than the heat of the reaction between chemical explosives. The heat of the reaction is determined by the energy of enhancement of the metallic bond between Ni and Al atoms in the intermetallic compound compared to pure Ni and Al metals.

In this work, we study experimentally and theoretically the laser modification of the Ni/Al multilayer structure (alternating nickel and aluminum layers, where the first layer is nickel). The possibility of partial or complete removal of upper layers of the structure under the variation of the energy of femtosecond laser pulses is demonstrated. The performed numerical simulation shows good agreement of the calculated depth and threshold of the spallation with our experimental data. To simulate ablation processes in multilayer structures under the action of femtosecond laser pulses, we use for the first time a two-temperature hydrodynamic code which allows obtaining new data on the propagation of acoustic perturbations, anomalous behavior of electron thermal flux, phase composition of layers at the time of rupture, and the magnitude and localization of the corresponding tensile stresses.

The authors of the preceding studies cited above usually performed only experiments. If works included calculations, nanolaminates were simulated using either molecular dynamics [20, 24] (target consisted of one or two layers) or a two-temperature model in one- or two-dimensional geometry [17, 25, 26] but disregarding hydrodynamic phenomena. Meanwhile, as will be shown below, hydrodynamic phenomena play a decisive role in the destruction of the target (thermomechanical ablation).

LASER EXPERIMENT

We study a Ni/Al multilayer sample with a total width of 1.28 μm consisting of two upper 46-nm Ni(1) and 50-nm Al(2) layers, 28 alternating 28-nm Ni and Al layers, and the base 400-nm Ni layer. This structure was deposited on a 120-μm quartz substrate. The modification of nanosized metal–metal bilayers was performed by means of the localized irradiation by linearly polarized pulses of an ytterbium laser with a duration of 270 fs at a wavelength of 1028 nm. The laser beam was incident normally on the surface of the sample and was focused by a 20× micro-objective on a spot with a Gaussian spatial distribution with a diameter of 3 μm at a level of $1/e$.

The surface of the sample was irradiated through air by single laser pulses in the wide energy density range of $F_0 = 0.4–21$ J/cm^2 (where F_0 is the energy density of incident laser radiation in the center of the focal spot). The modified regions of the target were studied with a Veeco Multimode 5 atomic force microscope in the contact regime and an Olympus optical microscope. The depth resolution of the atomic force microscope was 0.05 nm. The energy of incident laser pulses was measured with an accuracy of 2%. The experiments were performed on the equipment of the Shared Usage Center Femtosecond Laser Complex, Joint Institute for High Temperatures, Russian Academy of Sciences.

Figure 1 shows the measured morphology of the modified surface of the Ni/Al multilayer structure after irradiation by a single femtosecond laser pulse with different energy densities F_0. The right panels present optical microscopy images of craters on the surface.

At an energy density of laser radiation of 0.42 J/cm^2, the partial ablation of the upper Ni(1) layer occurs in the form of a two-level concentric crater with a depth of 30 nm in the center and of 19 nm at the periphery (Fig. 1a). The crater is surrounded by a rim characteristic of the thermomechanical ablation of metals and is due to the cavitation expansion of the melt near the ablation threshold [27]. As the energy density of femtosecond laser pulses increases (Fig. 1b), the depth of the central region of the crater increases to 46 nm, reaching the interface between the Ni(1) and Al(2) layers. At the same time, the depth of the outer crater remains at 19 nm.

With a further increase in F_0 (Fig. 1c), the structure of the crater becomes three-level. The depth in the central part of the crater is about 71 nm, and the bottom of this part is located inside the Al(2) layer. The depths of two peripheral levels remain approximately unchanged. The light region in the central part of craters on optical images (Figs. 1a, 1b) is due to a high reflectivity of aluminum at the interface between the layers. The dark central region in Fig. 1c is obviously due to a lower reflectivity of the nanostructured surface of aluminum [28] after rupture inside the Al(2) layer. The same reason is responsible for the dark outer ring in Figs. 1a–1c, which is due to ablation inside the Ni(1) layer.

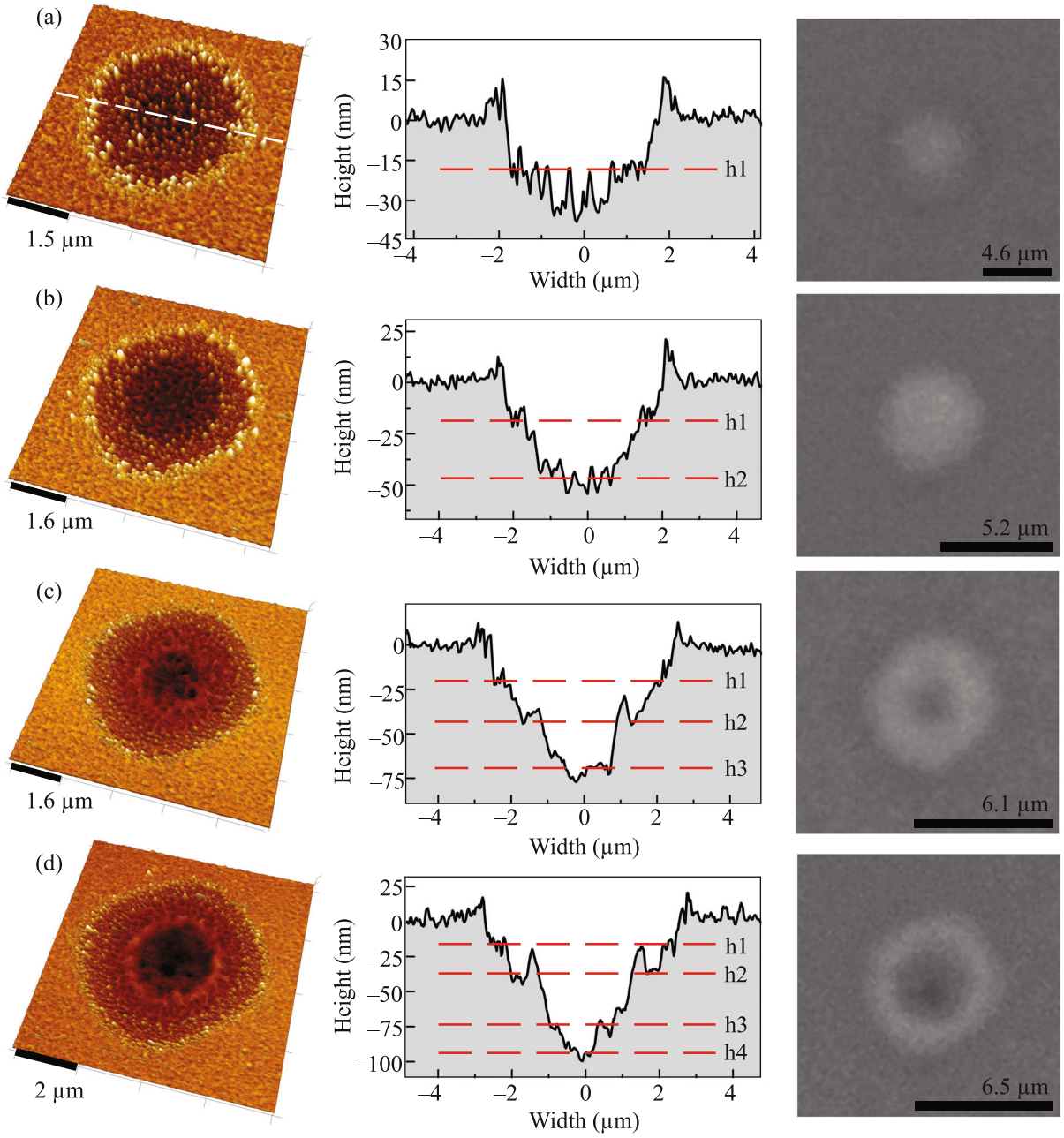

Fig. 1. (Color online) Modification of the multilayer structure after irradiation by a single femtosecond laser pulse with the energy densities F_0 = (a) 0.42, (b) 1.07, (c) 2.27, and (d) 3.12 J/cm^2. Left panels are atomic force microscopy scans, middle panels are the cross sections of craters, and right panels are their optical images.

According to atomic force microscopy data, the initial roughness of the surface of the sample was R_a = 4.6 nm. The roughness at the Ni(1)/Al(2) rupture interface is only 30% larger than the initial value (Table 1). The roughness at the Al(2)/Ni(3) rupture interface is approximately the same, but its exact measurement is complicated because of the small area of the spallation.

Figure 2 shows the dependences of the transverse size of multilevel craters on the logarithm of the energy of femtosecond laser pulses. These dependences are used to determine the threshold values and the parameters of a Gaussian beam using a known method [29]. The squares, circles, and triangles correspond to spallation inside the upper Ni(1) layer, at the interface between the Ni(1) and Al(2) layers, and inside the

Table 1. Ablation thresholds F_a^{in} in terms of the incident fluence, spallation depth h, and roughness R_a at shear boundaries

	F_a^{in}, J/cm^2	h, nm	R_a, nm
F_{a1}^{in} inside the Ni(1) layer	0.14	19 ± 3	8.6 ± 0.8
F_{a2}^{in} between the Ni(1) and Al(2) layers	0.73	46 ± 5	6.0 ± 0.2
F_{a3}^{in} inside the Al(2) layer	1.83	71 ± 3	4
F_{a4}^{in} between the Al(2) and Ni(3) layers	3.11	96 ± 3	5

Al(2) layer, respectively. The measured depths and thresholds at the modification of the multilayer structure are summarized in Table 1.

Table 1 presents the ablation thresholds are given in terms of the incident energy density (fluence). According to [30, 31], the coefficient of reflection of 1028-nm radiation normally incident on the Ni surface is $R = 0.73$. Correspondingly, the first threshold in the absorbed energy density will be $F_{a1}^{abs} = (1 - R)F_{a1}^{in} \approx 0.04$ J/cm^2; the superscripts "in" and "abs" mark the energies F_{a1}^{in} and F_{a1}^{abs} *incident* on the target and *absorbed* in it, respectively. It is noteworthy that the presented F_{a1} for our laminate is one-third of the ablation threshold for the bulk nickel target measured in [32]. The reason for a low first threshold of spallation inside layer Ni(1) will be considered below.

NUMERICAL SIMULATION

A fast laser heating of the metal by femtosecond laser pulses results in a large excess of the electron temperature T_e above the ion temperature T_i (two-temperature system). In turn, this leads to a significant increase in the electron thermal conductivity (compared to single-temperature values from reference books) at times smaller than the characteristic time of electron–phonon heat exchange [33–35]. Furthermore, hydrodynamic processes of shear, compression, and tension of matter begin to play a significant role in phenomena at a high energy of laser radiation responsible for the ablation of the material of a target.

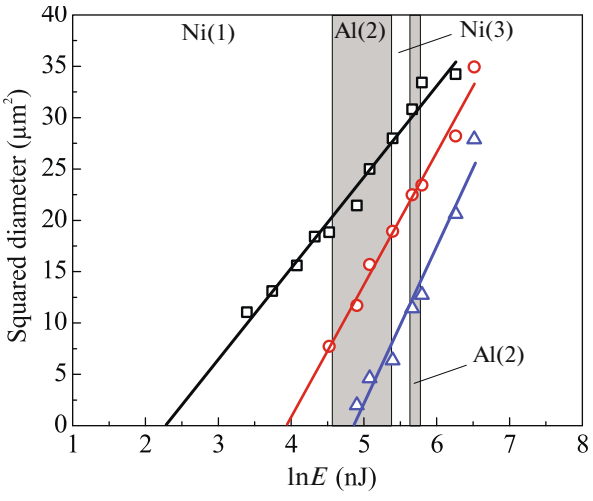

Fig. 2. (Color online) Squared diameter of multilevel craters on the surface of the Ni/Al structure versus the energy of femtosecond laser pulses.

The calculations of the laser modification of the Ni/Al multilayer structure given below are performed with our previously developed two-temperature hydrodynamic code; see, e.g., [36, 37]. In this work, we calculate only the first threshold F_{a1}^{abs} and the corresponding depth of the crater in the plastic approximation. A unified description of the solid and liquid phases is necessary because the melting and crystallization of the material occur.

The adequacy of the applied physical model can be estimated by comparing the calculations with the above experimental results. Such calculations (including hydrodynamic processes) for the multilayer target are performed for the first time. We are going to use this verified approach for the numerical simulation to determine the second threshold F_{a2}^{abs} and adhesion force at the interface between nickel and aluminum layers.

We compare the characteristics of nickel and aluminum significant for the description of ultrashort action.

First, the heat capacity $C_e(T_e, \rho)$ of the electron subsystem of nickel at normal density is an order of magnitude higher than that for aluminum. This is due to the structure of the electron spectrum of nickel $3d^{8-9}4s^{2-1}$ compared to aluminum $3s^2 3p^1$. The spectrum of electron states below and above the Fermi level in nickel is much denser than that for aluminum. Because of the difference in the heat capacity C_e, the electron temperature T_e in nickel is below than that in aluminum at the same electron energy density.

Second, the ion heat capacity of nickel C_i per unit volume is higher than that for aluminum by a factor of 1.5. If heat conduction processes are ignored, this rela-

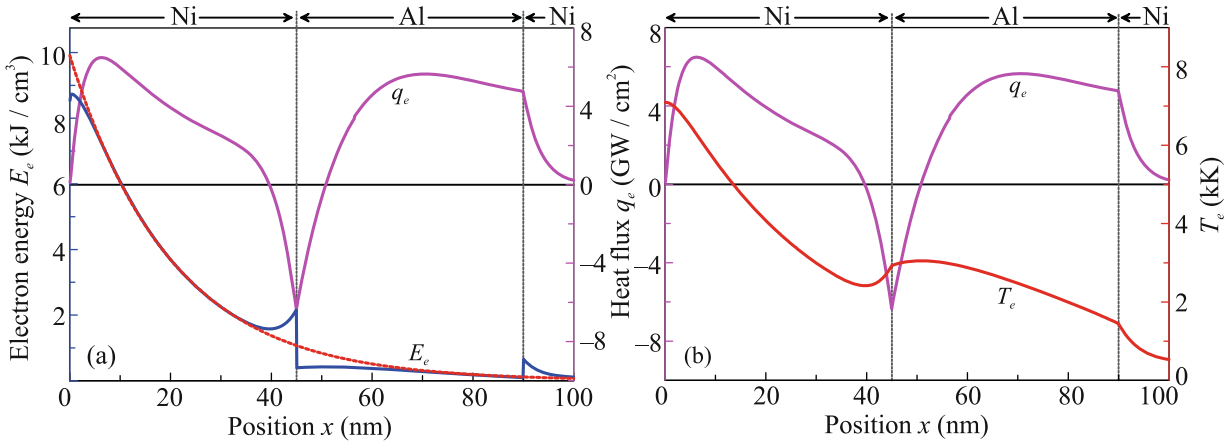

Fig. 3. (Color online) Target at the time $t = 0$ absorbs half the energy $F^{\text{abs}} = 40$ mJ/cm^2 assigned to it. (a) Red dotted line is the instantaneous profile of the dissipation power of the energy of the laser electromagnetic wave $I/\delta \propto \exp(-t^2/\tau_L^2)\exp(-x/\delta)$ W/cm^3 with power transfer to the energy of the electron subsystem. The violet line is the thermal flux q_e and the blue line is the electron energy. (b) Red line is the T_e profile. The nonmonotonic behavior of the temperature T_e is due to the inversion of the flux q_e.

tion is a reason for a higher ion temperature T_i in aluminum at the same ion energy density.

Third, nickel is much harder than quite soft aluminum whose acoustic impedance is one-third of that for nickel.

The mentioned difference between the heat capacities C_e is responsible for the anomaly of electron temperature profiles at the early stage (Fig. 3). It is seen that the ordinary behavior with a decrease in the temperature T_e toward the center of the target is violated and an inversion segment appears, where the electron heat flux $q_e = -\kappa\partial T_e/\partial x$ flows not toward the center of the target but in the opposite direction toward the frontal (i.e., irradiated) surface. The inversion of the flux is localized near the interface because the jump of the heat capacity C_e occurs at the interface. The violet lines in Figs. 3a and 3b show the instantaneous (at $t = 0$) flux profile q_e. The maximum of the inverse flux is located at the interface. The blue line corresponds to the instantaneous ($t = 0$) energy density profile. The red line in Fig. 3b is the electron temperature.

The time in the calculations is measured from the maximum of the intensity of the laser pulse $I(t) \propto \exp(-t^2/\tau_L^2)$, whose width at a level of $1/e$ is $2\tau_L = 100$ fs. To the time $t = 0$, half the absorbed energy of the femtosecond laser pulse F^{abs} is introduced in the target. Radiation is absorbed according to the Bouguer law $I(x,t) \propto \exp(-t^2/\tau_L^2)\exp(-x/\delta)$ with the relaxation length $\delta = 20$ nm. Figure 3 shows the variant with the absorbed energy $F^{\text{abs}} = 40$ mJ/cm^2. At the time $t = 0$, the nonmonotonic behavior of the temperature T_e is obtained in all calculations with $F^{\text{abs}} = 35$, 40, 50, and 60 mJ/cm^2.

The initial electron energy of nanolaminate $E_e(x, t = -\infty)$ at room temperature is much lower than the acquired energy $E_e(x, t = 0)$. The profiles I/δ [W/cm^3] (red points) and E_e [J/cm^3] (blue line) in Fig. 3a are matched artificially. It is clear that these profiles are similar, $E_e(x,t) = \int_{-\infty}^{t} dt' I(x,t')/\delta$, if energy transfers and bulk cooling in the medium are insignificant. Significant violation of similarity between I/δ and E_e is due to transfer of the absorbed energy from aluminum to nickel, although the heat release I/δ is continuous at the interface.

We note that the electron heat flux q_e is 1–10 GW/cm^2 (see Fig. 3), and the absorbed light flux intensity is two orders of magnitude larger. Thus, during the action of the laser pulse, the energy absorbed in the skin layer δ in unit time is two orders of magnitude larger than the energy removed because of the electron thermal conductivity. Consequently, first, the electron temperature increases during the pulse and, second, the removal of heat from the sink layer continues after the end of the pulse. However, the flux q_e cannot transfer a noticeable amount of energy from nickel to the underlying aluminum layer at our thickness of the nickel layer (the first layer absorbing light); see the temperature profile T_e in Fig. 4 at a time of 2 ps. The reason is that electron–ion relaxation in nickel proceeds in the time $t_{\text{eq}} \approx 3$–4 ps. After that, the electron thermal conductivity decreases significantly. For this reason, noticeable heating of the Al(2) aluminum layer by heat from the Ni(1) layer is

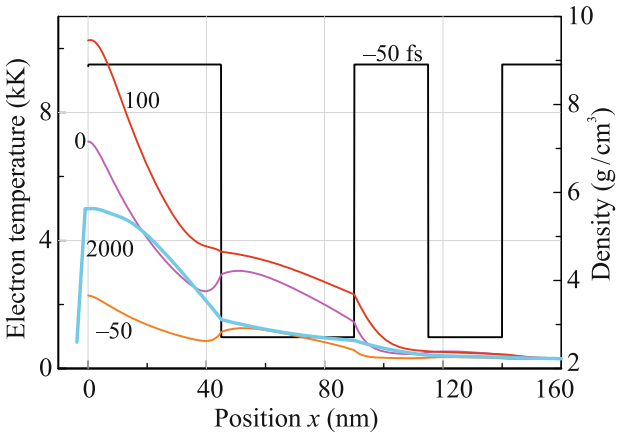

Fig. 4. (Color online) Step black line is the density profile at the time $t = -50$ fs. The other lines are the electron temperature profiles $T_e(x,t)$ at time in femtosecond marked next to the lines, $F^{abs} = 40$ mJ/cm^2. The electron temperature profile evolves such that the nonmonotonicity disappears and a small amount of energy is transferred to the Al(2) layer owing to the thermal conductivity.

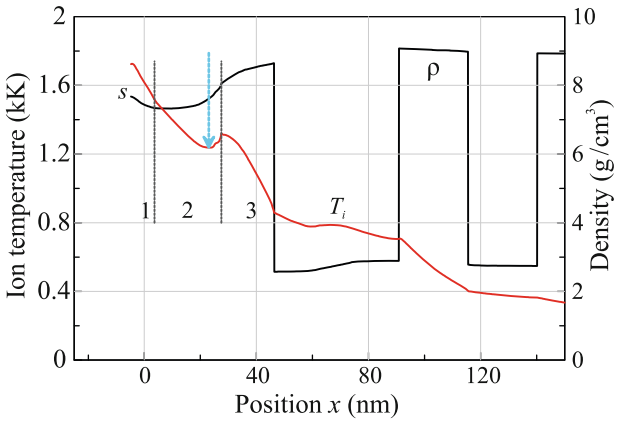

Fig. 5. (Color online) Phase states of the layer: (1) melt, (2) mixture of the liquid and solid phases; the crystal phase is to the right of the vertical straight line separating layers 2 and 3. The red and step black lines are the profiles of the ion temperature T_i and the density ρ; $t = 14$ ps, calculation with $F^{abs} = 40$ mJ/cm^2 and without the possibility of rupture of the material.

absent in a time about the duration of the acoustic stage $t_s = d_f/c_s \approx 10$ ps, where d_f is the thickness of the Ni(1) nickel layer and c_s is the speed of sound. The mechanical rupture occurs at the acoustic stage (if the energy F^{abs} is above the threshold). Further, the cooling of outer layers caused by transfer toward the center of the target does not affect the thickness h of the ablation-carried layer.

The degree of nonmonotonicity at early times is higher (see Fig. 4). Indeed, the ratio $\Delta T_e/T_e|_s$, where $T_e|_s$ is the temperature of the surface at the corresponding time and ΔT_e is the temperature difference between the local maximum and minimum of the T_e profile, which are located to the left and right of the nickel-aluminum interface, is 0.18 and 0.09 at the times $t = -50$ and 0 fs, respectively (see Fig. 4), where the times in femtoseconds are given next to the profiles. The anomalous (nonmonotonic) behavior of the temperature T_e is short-term because the light energy reaching aluminum through the nickel layer is low. The energy entering aluminum owing to the thermal conductivity is larger than that delivered by the electromagnetic wave. As soon as the first picosecond after ultrashort laser action, the electron temperature and electron energy flux profiles acquire an ordinary monotonic form (see Fig. 4).

The determining hydrodynamic motion begins at the acoustic stage at times of several picoseconds in the form of the propagation of the compression and rarefaction waves from the interface with vacuum inside the laminate. The rupture of the first nickel layer occurs at the fluence F_{a1} (see Table 1) when the tensile stress becomes higher the strength of nickel.

The phase composition of a material is important for the initiation of the process of destruction because the rupture strength of the material (thermomechanical ablation) under tension decreases significantly after melting [38, 39]. Figure 5 shows the phase state of the layers of the multilayer structure in a stage when the energy transfer from the electron subsystem to the ion one is almost completed. The boundary of the condensed phase is marked by the letter s. The evaporated material is to the left of this boundary. When the absorbed energy is $F^{abs} = 40$ mJ/cm^2, the amount of vapor is small, and its mass thickness is 0.9×10^{-7} g/cm^2, which is 0.02% of the mass of the first layer nickel. To the time shown in Fig. 5, the thickness of the vapor layer is approximately 15 nm. Digits 1 and 2 mark liquid and liquid–crystal mixture layers, respectively. If the energy $F^{abs} = 40$ mJ/cm^2 is uniformly distributed over the nickel layer with an initial thickness of 45 nm, this energy is enough to melt the layer and raise its temperature to several hundred degrees above the melting temperature.

The right boundary of the mixture (layer 2) in Fig. 5 moves to the right at a velocity of 450 m/s. A small decrease in the temperature to the left from this boundary is due to melting and extension of the material (extension results in a decrease in the melting temperature $T_m(p)$ and, consequently, facilitates melting [40]). The minimum temperature marked by the cyan arrow in Fig. 5 is exactly at the minimum pressure on the red line in Fig. 6 (the red line is the calculation disregarding the possibility of the rupture of the material). Our hydrodynamic simulation with a wide mixture region (at picosecond times) is in good agreement with molecular dynamics calculations including the kinetics of melting [40, 41]. The Stefan approximation

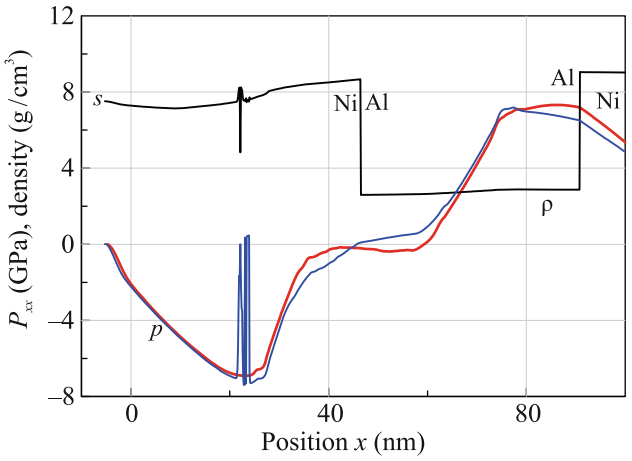

Fig. 6. (Color online) (Red and blue lines) Pressure and (black line) density profiles in the Euler coordinate x at the time $t = 14$ ps and $F^{abs} = 40$ mJ/cm^2. The density undergoes jumps at the interfaces between Ni and Al. The red line is obtained with the code neglecting rupture, whereas the blue and black lines calculated with the code include rupture. The density in the rupture region begins to decrease sharply and tensile stress vanishes (unloading at rupture). Rupture occurs at the minimum of the red line.

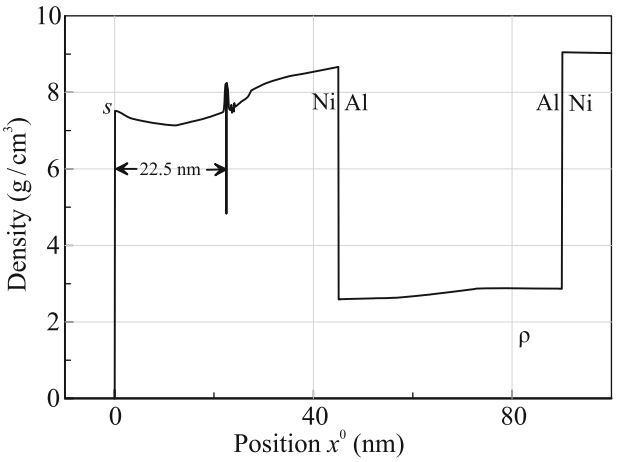

Fig. 7. Version with allowance for rupture. Beginning of the formation of rupture. The instantaneous (at $t = 14$ ps) density profile in the Lagrange coordinate x^0, which makes it possible to exactly determine the mass of the separated (ablated) layer $\rho_0 \times 22.5$ nm, where ρ_0 is the initial density of nickel.

is inapplicable in this situation; in this approximation, there is no mixture, the melting front is thin, and the difference of the temperature gradient is equal to the velocity of motion of the front in the material multiplied by the heat of fusion per unit volume. Our approach involves broadband equations of states of nickel and aluminum [42–44], which allow accurately including the heats of evaporation and fusion at phase transformation in the through calculation regime.

Figure 6 shows the (black line) density and (blue and red lines) pressure profiles. The red and blue lines are obtained in the calculations without and with the possibility of rupture, respectively. Figures 5–7 are presented for comparison of two versions of calculations. The density profiles obtained in two versions of calculations are shown in Figs. 5 and 6 (black lines with steps).

As seen, the two versions differ in a very remarkable feature associated with internal rupture in the nickel layer. At a time of 14 ps, the rupture only nucleates and the rupture region is very narrow. Unloading shock waves propagate from the rupture to the right and left: unloading of the tensile stress occurs "stepwise" from a finite value to zero. In nature, this is due to fast (subpicosecond) development of the nucleation process. In the calculation, the rupture occurs in one time step of integration when the rupture criterion is reached. Unloading shock waves are also called spall pulses. The material outside shocks "does not" know about rupture. Rupture occurs at the minimum pressure (on the red line in Fig. 6). This minimum is associated with the minimum temperature in Fig. 5 marked by marked by the cyan arrow.

According to [38], the strength of the liquid phase σ decreases with increasing temperature; near the melting temperature T_m at an actual tension rate of about 3×10^9 s^{-1}, it is about 8 GPa, which is in agreement within an error of 10% with the calculated tensile stresses in Fig. 6. More accurate determination of the strength requires additional molecular dynamics calculations. The mass thickness of the spall plate is determined in Fig. 7, where the Lagrange coordinate x^0 is the spatial position of material particles with respect to the interface with vacuum before laser irradiation. The numerical data obtained from the energy, $F_{al}^{abs} = 0.04$ J/cm^2 (at the coefficient of reflection R), and depth, $h = 22.5$ nm, rupture thresholds (Fig. 7) are in good agreement with the experimental result $h = (19 \pm 3)$ nm (see Table 1).

CONCLUSIONS

Features of the modification of a multilayer structure consisting of a sequence of nickel and aluminum nanolayers irradiated by femtosecond laser pulses have been studied. It has been found experimentally that the first rupture occurs inside the upper nickel layer rather than at the interface between two upper layers. The reason is the interference of rarefaction waves propagating toward each other from the free surface of the sample and from the interface between nickel and aluminum. The simulation indicates that nickel in the region of the maximum tension is in this case in the state of a two-phase mixture. The calculated first

threshold and spallation depth are in good agreement with the respective experimental values. The inverse behavior of the electron thermal flux near the interface between upper layers at the initial two-temperature stages has been shown theoretically. This phenomenon weakens the heating of aluminum.

FUNDING

S.A. Romashevskiy, S.I. Ashitkov, P.S. Komarov, and E.V. Struleva (experimental part) and V.A. Zhakhovsky, N.A. Inogamov, and A.N. Parshikov (theoretical part) acknowledge the support of the Russian Science Foundation (project no. 19-19-00697) and the Ministry of Science and Higher Education of the Russian Federation (project no. 075-15-2020-801). V.A. Khokhlov and Yu.V. Petrov (hydrodynamic simulation) acknowledge the support of the Ministry of Science and Higher Education of the Russian Federation (agreement no. 075-15-2020-785 with Joint Institute for High Temperatures, Russian Academy of Sciences).

REFERENCES

1. J. A. Syed, S. Tang, and X. Meng, Sci. Rep. **7**, 4403 (2017).
2. S. J. Bull and A. M. Jones, Surf. Coat. Technol. **78**, 173 (1996).
3. M. M. Barysheva, A. E. Pestov, N. N. Salashchenko, M. N. Toropov, and N. I. Chkhalo, Phys. Usp. **55**, 681 (2012).
4. V. V. Temnov, Nat. Photon. **6**, 728 (2012).
5. V. V. Temnov, C. Klieber, K. A. Nelson, T. Thomay, V. Knittel, A. Leitenstorfer, D. Makarov, M. Albrecht, and R. Bratschitsch, Nat. Commun. **4**, 1468 (2013).
6. C.-Yu Chen and T.-Li Chang, Microelectron. Eng. C **143**, 41 (2015).
7. B. Gakovic, C. Radu, M. Zamfirescu, B. Radak, M. Trtica, S. Petrovic, P. Panjan, F. Zupanic, C. Ristoscu, and I. N. Mihailescu, Surf. Coat. Technol. **206**, 411 (2011).
8. M. Ulmeanu, M. Filipescu, N. D. Scarisoreanu, G. Georgescu, L. Rusen, and M. Zamfirescu, Appl. Phys. A **104**, 247 (2011).
9. N. L. LaHaye, J. Kurian, P. K. Diwakar, L. Alff, and S. S. Harilal, Sci. Rep. **5**, 13121 (2015).
10. N. A. Inogamov, V. V. Zhakhovskii, S. I. Ashitkov, Yu. V. Petrov, M. B. Agranat, S. I. Anisimov, K. Nishikhara, and V. E. Fortov, J. Exp. Theor. Phys. **107**, 1 (2008).
11. M. E. Povarnitsyn, T. E. Itina, M. Sentis, K. V. Khishchenko, and P. R. Levashov, Phys. Rev. B **75**, 235414 (2007).
12. P. A. Danilov, D. A. Zayarny, A. A. Ionin, S. I. Kudryashov, Ch. T. Kh. Nguen, A. A. Rudenko, I. N. Saraeva, A. A. Kuchmizhak, O. B. Vitrik, and Yu. N. Kul'chin, JETP Lett. **103**, 549 (2016).
13. N. A. Smirnov, S. I. Kudryashov, P. A. Danilov, A. A. Rudenko, A. A. Ionin, and A. A. Nastulyavichus, JETP Lett. **108**, 368 (2018).
14. N. A. Inogamov, V. A. Khokhlov, and V. V. Zhakhovskii, JETP Lett. **108**, 439 (2018).
15. S. A. Romashevskiy, P. A. Tsygankov, S. I. Ashitkov, and M. B. Agranat, Appl. Phys. A **124**, 376 (2018).
16. B. Gaković, S. Petrović, C. Albu, M. Zamfirescu, P. Panjan, D. Milovanović, G. Popescu-Pelin, and I. N. Mihailescu, Opt. Laser Technol. **89**, 200 (2017).
17. B. Gaković, G. D. Tsibidis, E. Skoulas, S. M. Petrović, B. Vasić, and E. Stratakis, J. Appl. Phys. **122**, 223106 (2017).
18. S. I. Kudryashov, B. Gakovic, P. A. Danilov, S. M. Petrovic, D. Milovanovic, A. A. Rudenko, and A. A. Ionin, Appl. Phys. Lett. **112**, 023103 (2018).
19. S. Petrović, B. Gaković, M. Zamfirescu, C. Radu, D. Peruško, B. Radak, C. Ristoscu, S. Zdravković, C. L. Luculescu, and I. N. Mihailescu, Appl. Surf. Sci. **417**, 16 (2017).
20. A. Naghilou, M. He, J. S. Schubert, L. V. Zhigilei, and W. Kautek, Phys. Chem. Chem. Phys. **21**, 11846 (2019).
21. R. D. Murphy, B. Torralva, and S. M. Yalisove, Appl. Phys. Lett. **102**, 181602 (2013).
22. J. Roth, H.-R. Trebin, A. Kiselev, and D.-M. Rapp, Appl. Phys. A **122**, 500 (2016).
23. V. Turlo, O. Politano, and F. Baras, J. Appl. Phys. **121**, 055304 (2017).
24. N. A. Inogamov, V. V. Zhakhovsky, V. A. Khokhlov, Yu. V. Petrov, and K. P. Migdal, Nanoscale Res. Lett. **11**, 177 (2016).
25. S. Zhou, K. Zhao, and H. Shen, Opt. Laser Technol. **132**, 106495 (2020).
26. V. V. Shepelev and N. A. Inogamov, J. Phys: Conf. Ser. **946**, 012010 (2018).
27. S. I. Ashitkov, N. A. Inogamov, V. V. Zhakhovskii, Yu. N. Emirov, M. B. Agranat, I. I. Oleinik, S. I. Anisimov, and V. E. Fortov, JETP Lett. **95**, 176 (2012).
28. S. I. Ashitkov, S. A. Romashevskii, P. S. Komarov, A. A. Burmistrov, V. V. Zhakhovskii, N. A. Inogamov, and M. B. Agranat, Quantum Electron. **45**, 547 (2015).
29. J. M. Liu, Opt. Lett. **7**, 196 (1982).
30. M. A. Ordal, R. J. Bell, R. W. Alexander, L. L. Long, and M. R. Querry, Appl. Opt. **2**, 744 (1987).
31. A. D. Rakić, A. B. Djurišić, J. M. Elazar, and M. L. Majewski, Appl. Opt. **37**, 5271 (1998).
32. E. V. Struleva, P. S. Komarov, and S. I. Ashitkov, High Temp. **57**, 659 (2019).
33. N. A. Inogamov, V. V. Zhakhovsky, S. I. Ashitkov, V. A. Khokhlov, V. V. Shepelev, P. S. Komarov, A. V. Ovchinnikov, D. S. Sitnikov, Yu. V. Petrov, M. B. Agranat, S. I. Anisimov, and V. E. Fortov, Contrib. Plasma Phys. **51**, 367 (2011).
34. Yu. V. Petrov, N. A. Inogamov, and K. P. Migdal, JETP Lett. **97**, 20 (2013).

35. Yu. V. Petrov and N. A. Inogamov, JETP Lett. **98**, 278 (2013).
36. S. I. Anisimov, N. A. Inogamov, Yu. V. Petrov, V. A. Khokhlov, V. V. Zhakhovskii, K. Nishihara, M. B. Agranat, S. I. Ashitkov, and P. S. Komarov, Appl. Phys. A **92**, 939 (2008).
37. N. A. Inogamov, V. V. Zhakhovskii, and V. A. Khokhlov, J. Exp. Theor. Phys. **127**, 79 (2018).
38. A. E. Mayer and P. N. Mayer, J. Appl. Phys. **118**, 035903 (2015).
39. P. N. Mayer and A. E. Mayer, J. Appl. Phys. **124**, 035901 (2018).
40. B. J. Demaske, V. V. Zhakhovsky, N. A. Inogamov, and I. I. Oleynik, Phys. Rev. B **87**, 054109 (2013).
41. N. A. Inogamov, V. V. Zhakhovskii, S. I. Ashitkov, V. A. Khokhlov, Yu. V. Petrov, P. S. Komarov, M. B. Agranat, S. I. Anisimov, and K. Nishihara, Appl. Surf. Sci. **255**, 9712 (2009).
42. A. V. Bushman, G. I. Kanel', A. L. Ni, and V. E. Fortov, *Intense Dynamic Loading of Condensed Matter* (Taylor and Francis, Washington, D.C., 1993).
43. K. V. Khishchenko, S. I. Tkachenko, P. R. Levashov, I. V. Lomonosov, and V. S. Vorobev, Int. J. Thermophys. **23**, 1359 (2002).
44. I. V. Lomonosov, Laser Part. Beams **25**, 567 (2007).

Translated by R. Tyapaev